# A locally resolved investigation on direct methanol fuel cell uneven components fading: local cathode catalyst layer tuning for homogeneous operation and reduced degradation rate

*C. Rabissi[a]\*, M. Zago[a], P. Gazdzicki[c], L. Guétaz[d], S. Escribano[d], L. Grahl-Madsen[b], A. Casalegno[a]*

*[a] Politecnico di Milano, Department of Energy, via Lambruschini 4, 20156 Milano, Italy.*

*[b] EWII Fuel Cell A/S, Emil Neckelmanns Vej 15 A&B, DK-5220 Odense, Denmark*

*[c] German Aerospace Center (DLR), Institute of Engineering Thermodynamics, Pfaffenwaldring 38-40, 70569 Stuttgart, Germany*

*[d] Université Grenoble Alpes, CEA, LITEN, 17 rue des Martyrs, 38054 Grenoble, France*

*\*corresponding author: claudio.rabissi@polimi.it*

**Abstract**

Durability issues of direct methanol fuel cell still hinder technology widespread commercialization; uneven aging of MEA components, generally harsher in air outlet region, is known to exasperate overall performance degradation. In a previous work, the authors selected a stable cathode electrode, demonstrated to fade homogenously: uneven water-related limitations, such as dehydration and flooding, were revealed to locally worsen performance at cathode inlet and outlet regions, leading to current redistribution. Aiming to reduce degradation rate, in this work homogeneous current distribution during operation is pursued by tuning MEA properties to meet local operating conditions. A properly improved 1D+1D physical model is used to support the development of a gradient MEA, featuring 1.6 mg·cm$^{-2}$ and 0.8 mg·cm$^{-2}$ of catalyst and ionomer respectively at inlet/outlet and center regions of cathode electrode. Tests based on custom macro-segmented cell demonstrated 55% more homogeneous current distribution, controllable during operation by means of cathode air

stoichiometry. 500 h degradation test revealed 70% decreased degradation rate from uniform MEA (11 µV·h⁻¹) with a homogenous fading of performance. A 18% lower Pt nanoparticle growth at cathode outlet and limited ionomer degradation at cathode inlet were identified by ex-situ analyses (TEM and XPS), indicating locally mitigated fading mechanisms.

**Keywords:** Direct methanol fuel cell; segmented cell; heterogeneity; local degradation; gradient MEA; ex-situ.

## 1    Introduction

Thanks to the employment of a high energy density liquid fuel, permitting convenient and quick recharging [1–3], direct methanol fuel cell (DMFC) is a promising technology for stationary and portable power production from very small to medium scale (e.g. portable electronics to off-grid applications) as well as for light and industrial vehicular sectors. However, such applications require at least several thousand hours of lifetime without any relevant degradation of performance; unfortunately, durability issues of this technology [4] still constitute a critical point which limit technology widespread commercialization. Also, other important drawbacks of this technology are generally related to high cost of the materials together with low efficiency and power density compared with hydrogen PEMFC.

DMFC performance degradation is thoroughly investigated in the literature, distinguishing the irrecoverable mechanisms [5–8], related to permanent alterations of catalyst layers (CL), gas diffusion layers (GDL) and polymer electrolytic membrane (PEM) properties, from temporary mechanisms [9–13]. In particular, cathode CL electrochemical surface area (ECSA) loss is known to be mainly related to electrochemical Ostwald ripening mechanism, platinum and ruthenium dissolution, migration and redeposition, together with carbon support corrosion [14–16].

Recently, locally resolved measurements and local post-mortem analysis [4,17–20] revealed the development of the onset of heterogeneity of degradation in DMFC samples, particularly stronger in terms of ECSA loss at cathode outlet region; a strong effort is being put in properly understanding the determining mechanisms. Despite segmented cell-based works are increasing in number [21–28], few works about DMFC degradation correlate local performance analysis during ageing with local degradation measured by ex-situ analysis, i.e. transmission electron microscopy (TEM) and X-Ray photoelectron spectroscopy (XPS), limiting results reliability and generality.

In a previous work [29], aiming to provide a combined investigation of heterogeneity of both performance and aging, the authors focused on DMFC heterogeneous degradation. Suspecting that the combination of cycling cathode operation together with increased water content promote electrochemical Ostwald ripening mechanism localized at cathode outlet region, a highly graphitized carbon supported cathode catalyst layer (CCL) component was selected, demonstrating strong stability in AST testing in presence of high water content. The so-called *uniform* MEA (in the following, UNF-MEA) was tested by means of an appositely developed macro-segmented cell (m-SFC) setup both in steady state and in degradation testing including ex-situ analysis. Uneven and redistributing performance over time was revealed; current density heterogeneous distribution was mostly due to water related limitations, leading to dehydrated as well as flooded regions, which locally increase the performance loss respectively at cathode inlet and outlet regions despite having reached an homogeneous ECSA loss. Hence, aiming to achieve homogeneous performance fading, MEA components properties would have to be locally adapted depending on the locally varying operating conditions of each CCL region (e.g. oxygen and water concentration, pressure, temperature), that are leading to locally varying performance limitations; on this, modelling simulations can give fundamental

indications. However, modelling analyses dealing with local performance investigation found in the literature [30–32] generally lack of rigorous and experimental validation, reducing the reliability of model results or limiting model prediction capabilities.

Based on results obtained in [29], the most critical components to focus on for the local properties optimization could be either CCL and GDL, both in terms of formulation and microstructure, to face locally dehydrating as well as flooding conditions. In literature, several studies on PEMFC optimization [33–38] were identified as useful to obtain insights helping the optimization strategy to be pursued in this work, among which very few discuss DMFC technology. However, these works often discuss simplified MEA geometries, seldom correlating modeling simulations together with experimental validation, hence lacking in representativeness of real operation and validation of the findings. The most promising strategy to be pursued, also considering manufacturing capability, has been identified in a compositional optimization of cathode CL formulation, in order to locally adapt operation to the different water and oxygen relative availability. Hence, in this work catalyst, ionomer and carbon loading will be locally shaped to promote operation in the performance limited regions identified, e.g. cathode inlet and outlet [29]. Local catalyst loading profile will be tuned by means of physical modelling simulation, aiming to a uniform current density distribution at the nominal operating point. Then, manufacturing and testing the optimized component will permit to demonstrate the impact on current distribution and durability of such local modification, strengthened by means of aged MEA ex-situ analyses.

## 2    Experimental and modelling methodology

### 2.1    MEA samples and testing hardware

Experiments are performed on 25 cm$^2$ DMFC MEAs manufactured by EWII Fuel Cells A/S. Analogously to [29], anode catalyst layer (ACL) is loaded with 1.8 mg·cm$^{-2}$ (PtRu alloy), while cathode catalyst layer (CCL) is provided with locally variable catalyst and ionomer loading, as discussed in section 4.1, corresponding to 1.2 mg·cm$^{-2}$ (Pt) average. For CCL, a highly graphitized carbon support with 0.5 Pt:C ratio is adopted consistently with [29], where the stability of this component was discussed in AST and DMFC operation.  On both sides Sigracet® SGL35DC GDLs  (thickness 325 μm, 20% PTFE content) provided with microporous layer (MPL) are used, while membrane is Nafion® 115 (127 μm thick).

The local experimental setup, thoroughly discussed in [29] and briefly summarized in the following, permits local detailed analysis of performance and degradation. A macro-Segmented Fuel Cell (m-SFC) hardware [29] is utilized in the experimental activity, featuring an active full control on four macro-regions of the cell. It enables complete electrochemical characterization of each segment while limiting internal border effects, avoiding crosscurrents and reciprocal interference between segments; the limited invasiveness of the setup has been demonstrated in [29]. A picture of the m-SFC setup is reported in the supplementary materials.

### 2.2    Operating conditions and testing protocols

As indicated by the MEA manufacturer, nominal current density and cell operating temperature are respectively 0.25 A·cm$^{-2}$ and 75°C. Anode is fed with 1.0 M methanol solution at constant stoichiometry $\lambda_A$=6 at 0.25 A·cm$^{-2}$, while cathode is fed with air fully humidified at ambient temperature (RH$_C$~10%) at increasing stoichiometry (from reference value of $\lambda_C$=3 at 0.25 A·cm$^{-2}$) as described in the following.

The m-SFC operates galvanostatically [29]: total current is divided by a 4-module electronic load (4x Chroma ATE 63610-80-20) between the four segments, aiming to homogeneous voltage value (limiting crosscurrents between consecutive segments). Degradation testing, described in section 4.3, is performed at nominal overall current density (0.25 A cm$^{-2}$) following a discontinuous protocol. Indeed, due to strong performance degradation rate experienced during continuous operation (up to several mV·h$^{-1}$ [39]), DMFC devices are often operated discontinuously [10–13]. Consistently with [29], in this work DMFC reference operating protocol consists of periods of 20 minutes galvanostatic operation interspersed by 1 minute of *refresh cycle*. Moreover, every 100 hours of operation a longer operation break, namely *full refresh* [4], is performed to fully recover temporary degradation, performing electrochemical diagnostics (described in section 2.5) and $\lambda_C$ value optimization. Indeed, as described in section 4.3, $\lambda_C$ is adjusted every 100 h during the break for diagnostics to maintain homogeneous current density distribution: short operation periods of 5 minutes each are performed increasing $\lambda_C$ up to 10% of the initial value, while measuring corresponding current density heterogeneity. The $\lambda_C$ value leading to the most homogeneous distribution is adopted for the subsequent 100 h operation.

The *refresh cycle*, thoroughly investigated in [12,13,39], consists of a sequence of an OCV and a cathode air feeding interruption, intended to recovery temporary degradation during operation. During air feed interruption period, cathode potential is expected to drop below 0.5 V to reduce platinum oxides [10] as discussed in the introduction.

The *full refresh* procedure, as in [4], consists of a ~16 h operation interruption under low mass flow of methanol solution (~0.3 g·min$^{-1}$) at anode electrode. Cell temperature is maintained at 75°C with both cathode inlet and outlet manifolds plugged to avoid excessive oxygen infiltrations.

### 2.3    Local in-situ electrochemical measurements

### 2.3.1    Local polarization curve with mass transport analysis

The acquisition of DMFC local polarization curve is composed of 9 single measurement points at different current densities, from 0.01 to 0.4 A·cm$^{-2}$. Each single acquisition point is performed setting the overall constant current density for the cell as described in section 2.2, measuring voltage and local current densities for 600 s. The measurement is performed with reactants at constant flow rates (corresponding to $\lambda_A$=6 and $\lambda_C$=3 stoichiometries at 0.25 A·cm$^{-2}$), in order to ensure the steady state operation. Aiming to investigate current density re-distribution, when described in the text, cathode air flow has been also increased from reference value to meet a stoichiometry of 3.25 and 6 at 0.25 A·cm$^{-2}$.

After each period, *refresh cycle* is performed to recover temporary degradation that may be developed during the measurement of the polarization curve itself, which could possibly affect the reliability of the measurement. The data obtained from each single acquisition point are elaborated as explained in [4], applying the method to the local current density value related to each of the four segments, in order to obtain the four local polarization curves.

Also DMFC anode polarization curves are measured in order to characterize the anode contribution to the permanent degradation, with the same methodology as in [4]: cathode is fed with hydrogen and used as a dynamic reference electrode (DHE). No local information is obtained with this technique.

### 2.3.2    Local Electrochemical Impedance Spectroscopy (EIS)

Local EIS are performed at 0.1 and 0.25 A·cm$^{-2}$ during the diagnostic polarization curves and at 0.25 A·cm$^{-2}$ during galvanostatic operation, using the modular electronic load (4x Chroma ATE 63610-80-20) featuring current waveform generation and high-speed acquisition.

The impedance is measured at 50 frequencies logarithmically spaced between 10 kHz and 50 mHz. In order to avoid any reciprocal interference between consecutive segments, accurate synchronous sinusoidal oscillation of the current density for all the segments is guaranteed. From the measurement of the four single local spectra, the overall cell impedance spectrum is calculated. As discussed in [29], measurement reliability is verified through the comparison of the overall calculated spectrum with that obtained measuring whole cell impedance with a single channel potentiostat (AUTOLAB 30N) provided with frequency response analyzer module (FRA). Measurement consistency is verified by a retrospective use of Kramers-Kronig transforms [40]: impedance values that do not satisfy such relations are discarded.

### 2.3.3 Cathode cyclic voltammetry (CV)

CV is used to estimate the ECSA value of CL, used as working electrode, whilst anode electrode is operated as an internal pseudo-DHE. 50 ml min$^{-1}$ of $H_2$ and $N_2$ are fed to anode and cathode compartments respectively, at 100%RH with 80°C cell temperature. The CV is measured scanning 5 times cathode potential between 0.08 V and 0.85 V with 0.05 V·s$^{-1}$ sweep rate, discarding the first cycle. Cathode ECSA is estimated considering the positive current density peak related to the hydrogen desorption [41]. The estimation assumes that cathode catalyst is covered by a monolayer of hydrogen with a charge density of 210 μC cm$^{-2}$.

In order to measure local ECSA, the same potential scan is simultaneously applied on each of the four segments of the m-SFC. Four hi-precision source-measure units modules (NI PXIe-4139), measuring the current related to each segment, is used to perform the measurement. From the four single local voltammograms, the overall cell voltammogram is calculated; its reliability has been verified by comparing it with the overall cell voltammogram measured with a single channel potentiostat (AUTOLAB 30N). Uncertainty for such measurement has been evaluated to be about 5% for the local spectra due to residual in-plane current exchange.

## 2.4 Ex-situ post-mortem analyses

### 2.4.1 X-Ray Photoelectron Spectroscopy (XPS) and X-Ray Diffraction (XRD)

XPS measurements have been performed using a ESCALAB 250 ultra-high vacuum (UHV) facility from Thermo Scientific with a base pressure of $1 \cdot 10^{-9}$ mbar. A Thermo Scientific XR4 x-ray sources (Al Kα radiation) operated at 300 W was used together with a hemispherical electron energy analyzer.

The samples were prepared by mechanically detaching the GDL (including MPL) from the catalyst coated membrane (CCM) using a scalpel. The so prepared CCMs and GDLs (MPL facing up) were mounted to a stainless steel sample holder by an electrically conductive double-sided carbon tape. The atomic concentrations of elements (at%) are calculated using sensitivity factors from Thermo Scientific Avantage Software.

XRD measurements were performed in reflection mode $\theta_1 = \theta_2$ using a Bruker D8 Discover GADDS diffractometer with a VÅNTEC-2000 area detector. A tuned monochromatic and parallel X-ray beam (Cu-Kα) was used.

### 2.4.2 Transmission Electron Microscopy (SEM and TEM)

MEA cross-sections were also analyzed by scanning electron microscopy (SEM) and transmission electron microscopy (TEM). Samples were taken from the MEA in the different selected regions (air inlet, air center and air outlet) and then embedded in epoxy resin. Cross-section samples were first prepared by mechanical polishing until mirror-like surface and then observed by SEM. Afterwards, thin sections were cut using a LEICA ultramicrotome and then investigated by TEM. SEM and TEM observations were respectively performed using a ZEISS LEO 1500 field emission gun (FEG) microscope and a FEI-Titan Ultimate microscope equipped with a Cs aberration probe corrector.

## 3   Model analysis

A previously developed 1D+1D DMFC physical based model [42–44] has been properly improved and subsequently utilized for the design of locally optimized CCL. The original model included the complete mass balance, considering two-phase flow at both anode and cathode; however, the effect of cathode flooding was introduced only as a reduction of DL diffusivity due to bulk and superficial DL pores obstruction [44]. Moreover, cathode CL dehydration effect was not considered and the reactants feeding was in co-flow configuration. A detailed description of the original model can be found in [42] for anode and in [43] for cathode electrodes, respectively. Since in [29] it was demonstrated that both cathode flooding and dehydration have a relevant influence on DMFC homogeneous operation and cathode degradation, in this work the original 1D+1D DMFC model is thus integrated with the following improvements:

- **Counter-flow reactants feeding**

In order to simulate operating conditions consistent with the experimental data, the ability of solving counter-flow reactants feeding has been firstly implemented.

In particular, introducing an iterative procedure based on the built-in Matlab® function *fgoalattain*, it is possible to effectively simulate counter-flow configuration keeping an acceptable computational time. The discretized simulation results are then averaged in geometrical consistence to the four macro-segments of the m-SFC hardware, in order to reproduce the local results coming from the experimental activity.

- **Cathode flooding**

The effect of flooding has been introduced as a reduction of oxygen diffusivity in CCL, adopting a correlation already proposed in the literature [45,46]:

$$D_{O_2}^{CCL} = D_{O_2,ref}^{CCL} \cdot \left(1 - s^{CCL}\right)^{1.5} \tag{1}$$

where $s^{CCL}$ is CCL liquid saturation, defined as:

$$s^{CCL} = \frac{C^{CCL}_{H_2O,liq} - C^{sat}_{H_2O}}{C^{CCL,max}_{H_2O,liq} - C^{sat}_{H_2O}} \qquad (2)$$

$C^{CCL,max}_{H_2O,liq}$ represents the maximum liquid water concentration in CCL, corresponding to the condition in which the water liquid pressure inside CCL reaches the DL breakthrough value [44,47] leading to liquid permeation through cathode DL; while $C^{sat}_{H_2O}$ indicates the saturation concentration. When water concentration is lower than its saturation value, $s^{CCL}$ is imposed equal to zero, indicating that no liquid water is present in the CCL. The value of $C^{CCL}_{H_2O,liq}$ along channel coordinate was already provided by the original 1D+1D DMFC model.

- **Cathode dehydration**

The effect of ionomer dehydration inside CCL has been described as a reduction of catalyst layer proton conductivity $\sigma^{CCL}$ in function of water content $\lambda^{CCL}$. Low $\lambda^{CCL}$ values imply proton conductivity reduction, leading to increased ohmic loss through CCL and this effect is calculated with a correlation reported in the literature [48,49]:

$$\sigma^{CCL} = \sigma^{CCL}_{ref} \cdot \left(0.46 \cdot \lambda^{CCL} - 0.25\right) \cdot \exp\left[-1190 \cdot \left(\frac{1}{T} - \frac{1}{298.15}\right)\right] \qquad (3)$$

The water content of CCL is defined as:

$$\lambda^{CCL} = \frac{EW \cdot C^{CCL}_{H_2O,liq}}{\rho_{dry}} \qquad (4)$$

where EW and $\rho_{dry}$ denote respectively the ionomer equivalent weight and the ionomer density in dry condition.

- **Local Pt loading distribution**

In order to design optimized/improved distribution of CCL catalyst and ionomer loading, the effect of modified local catalyst loading on the volumetric reaction rate of oxygen reduction reaction (ORR) is simulated with a direct proportional effect on the roughness factor [33], that

indicates the active surface area of catalyst specific to cell surface [$cm^2_{Pt} \cdot cm^{-2}$]. The resulting local reaction rate, following a Butler-Volmer kinetic, is:

$$R_{ORR,n} = i^*_{ORR} \cdot \frac{A_{Pt,n}}{A_{Pt,ref}} \cdot \left( \frac{C_{O_2}}{C_{O_2,ref}} \right) \cdot \left[ \exp\left( \frac{\alpha_{ORR} \cdot F}{R \cdot T} \cdot \eta_{ORR} \right) - \exp\left( \frac{-(1-\alpha_{ORR}) \cdot F}{R \cdot T} \cdot \eta_{ORR} \right) \right] \qquad (5)$$

where $n$ indicates the segment number, $A_{Pt}$ is the roughness factor measured in [$cm^2_{Pt} \cdot cm^{-2}$] and $i^*_{ORR}$ is the ORR exchange current density [$A\ cm^{-3}$]. For the sake of simplicity of manufacturing process and considering the m-SFC experimental hardware, the local modification of CCL loading has been discretized in four macro-areas, corresponding to those of the m-SFC segments.

Summarizing, the finalized 1D+1D DMFC model is thus able to simulate local I-V curves in counter flow-configuration, considering the effect of local flooding and dehydration in CCL. Such model, which does not aim to provide a detailed and exhaustive description of such complex phenomena, is expected to be an effective tool to provide a solid interpretation of the local experimental data and to design optimized CCL loading distribution.

## 4   Results and discussion

In the following, in consistency with [29], overall polarization curves and EIS spectra of the cell will be always represented by the black dotted data points, while the local measurement of the four segments will be indicated, moving from cathode inlet to outlet, respectively in green, blue, red and yellow solid curves.

Moreover, to evaluate the dispersion of current density distribution, a heterogeneity level index ε of the current density $i$ is defined as:

$$\varepsilon_i\ [\%] = \frac{\Delta i_{max}}{i} = \frac{i_{max} - i_{min}}{i} \qquad (6)$$

where $i$ is the current density of the overall cell, while $i_{max}$ and $i_{min}$ are the values of current density provided by the highest and the lowest performing segment, respectively.

## 4.1    Local MEA optimization

### 4.1.1    Model assisted design of local optimized CCL

The improved 1D+1D DMFC model is firstly validated with respect to the experimental data reported in [29], referring to a DMFC adopting a novel CCL material with uniform catalyst loading distribution (UNF-MEA); values of the most relevant model parameters are reported in the supplementary materials. As already proposed in [42,43], the validation approach considers four typologies of measure at the same time: anode polarization, overall polarization, methanol crossover and water content measured at cathode outlet, permitting in such way to consider the main physical phenomena with a reduced uncertainty. For the sake of shortness, in this work only simulations of polarization and anode polarization are reported: the comparison with the corresponding experimental data is depicted in Figure 1A.

As visible from the figure, experimental data are reproduced with acceptable accuracy; just for current density lower than 0.05 A·cm$^{-2}$, the difference between model and experiments becomes higher due to the Tafel kinetic assumption at anode electrode. This discrepancy is anyway acceptable since the aim of the model is to assist the DMFC optimization at nominal operating condition.
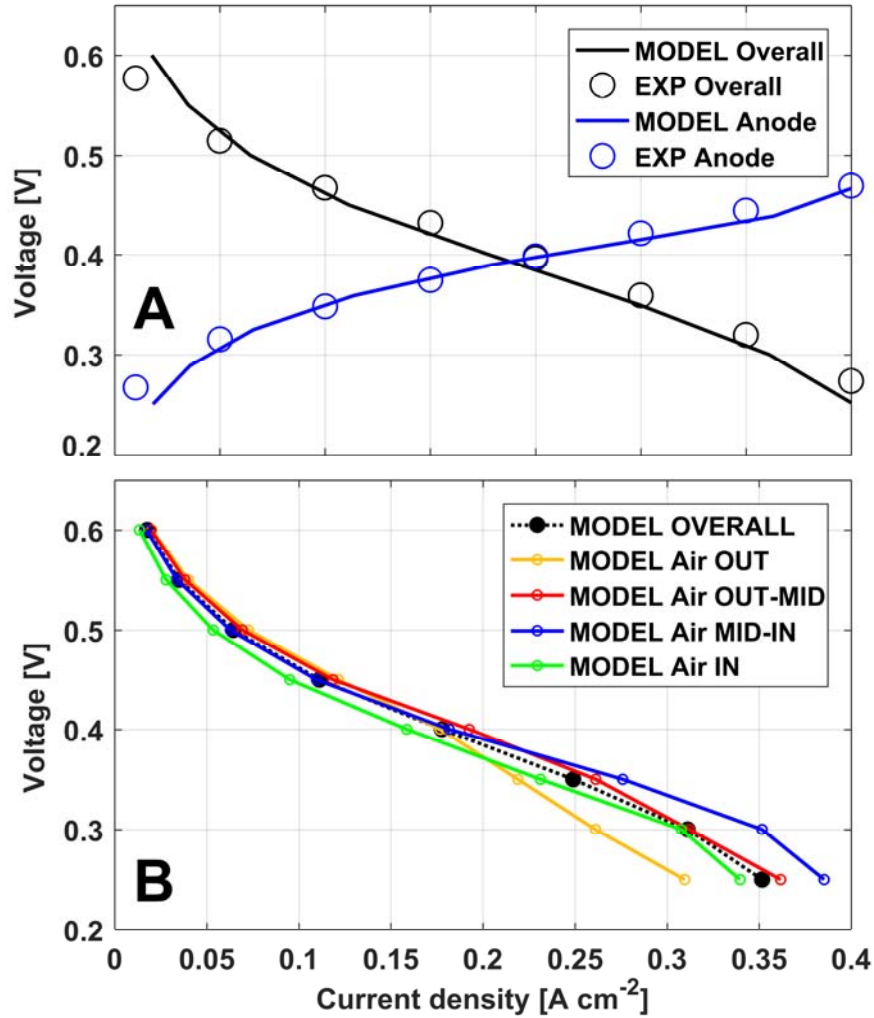
*Figure 1. A) Comparison between simulated and experimental I-V curves (from [29]) and B) corresponding simulated local I-V curves, at reference operating conditions*

Figure 1B shows the simulated local I-V curves in counter-flow nominal conditions, showing satisfying qualitative agreement with the corresponding experimental data reported in [29]. Cathode inlet (depicted in green in Figure 1B) presents low performance despite the local highest oxygen partial pressure among all the segments, while cathode outlet (depicted in yellow in Figure 1B) appears to be limited by mass-transport at high current density, quickly dropping in performance. Such behavior was discussed in [29] to be related respectively to

dehydration of polymer and flooding of CCL. Accordingly, an heterogeneity index of $\varepsilon_{i,MOD}$=22.8% is calculated at 0.25 A cm$^{-2}$, in good agreement with the experimental value, equal to $\varepsilon_{i,EXP}$=21.7% [29], confirming non-homogenous performance distribution.

It is worth to note that such model agreement with experimental local I-V curves is only reached after implementing dehydration and flooding effects as discussed in section 3, further confirming the importance of water distribution related mechanisms in determining local performance limitations. A better agreement between model and experiments could be obtained with the introduction of fitting parameters in the correlations describing flooding and dehydration effects, which is out of the scope of the work. Being the equations (2) and (4) directly obtained from the literature, the generality of the interpretation of the physical phenomena regulating local DMFC performance is further strengthened.

Demonstrated its reliability in properly simulating local DMFC performance, the model has been used to simulate the effects of gradients of cathode electrode catalyst and ionomer loading, in order to provide quantitative indications on the optimal distribution. The objective of the study is to quantify the CCL Pt loading in terms of the local values of $A_{Pt,1}$, $A_{Pt,2}$, $A_{Pt,3}$ and $A_{Pt,4}$, maintaining their sum equal to the reference value $A_{Pt,ref}$, which would lead to homogeneous current density distribution at the nominal operating point, as in the following:

$$minimize\ (\varepsilon_i, 0.25\ A\ cm^{-2})$$
$$\sum_{n=1}^{4} A_{Pt,n} = A_{Pt,ref} \tag{7}$$

where the local catalyst loading, identified in the roughness factor $A_{Pt,n}$, is parameterized in a functional form of the location y along the length of the fuel cell as four piecewise constant (positive) values, $A_{Pt,1\rightarrow4}$, consistently with m-SFC segments, as in the next equation:

$$A_{Pt} = \begin{cases} A_{Pt,1} & \left(0 < y < \dfrac{L}{4}\right) \\[2mm] A_{Pt,2} & \left(\dfrac{L}{4} < y < \dfrac{L}{2}\right) \\[2mm] A_{Pt,3} & \left(\dfrac{L}{2} < y < \dfrac{3L}{4}\right) \\[2mm] A_{Pt,4} & \left(\dfrac{3L}{4} < y < L\right) \end{cases} \qquad (8)$$

The results of such calculation lead to a "parabolic" gradient loading of catalyst and ionomer over MEA active area, whose distribution in the four macro-areas of the cell is reported in the scheme of Figure 2A. An increase to 1.6 mg·cm$^{-2}$ is required in CCL regions limited by dehydration or flooding (respectively <u>cathode inlet</u> and <u>outlet</u>), together with a corresponding decrease to 0.8 mg·cm$^{-2}$ at <u>cathode center</u> to keep unvaried the average loading to 1.2 mg·cm$^{-2}$. From now on, the parabolic gradient loaded MEA will be named PRB-MEA, distinguishing it from the standard uniform loaded UNF-MEA discussed in [29].
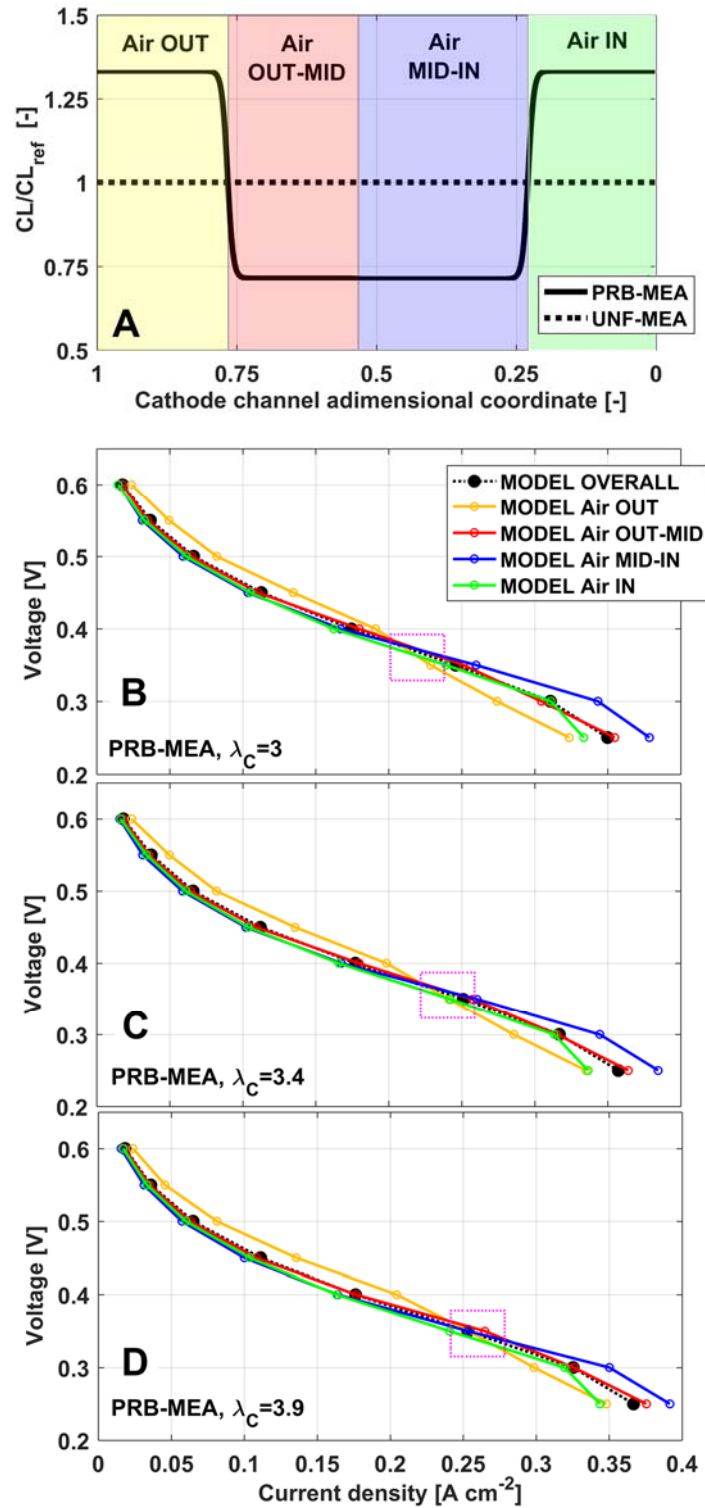
The simulated local I-V curves of the optimized PRB-MEA are reported in Figure 2B, where a promising heterogeneity level as low as $\varepsilon_i$=8% is calculated (at about 0.21 A·cm$^{-2}$). At <u>cathode inlet</u> (green curve in Figure 2B), the increase of catalyst and ionomer loading is confirmed to enhance local current density; as a direct effect, local dehydration is mitigated by a self-hydrating mechanism, due to the increased water production from ORR. However, such increase in local current density at <u>inlet</u>, leading to local increased oxygen consumption and water production, is counterproductive for performance at <u>cathode outlet</u> region (yellow curve in Figure 2B). Indeed, due to flooding onset, performance at <u>outlet</u> is calculated to drop when above 0.2 A cm$^{-2}$ even more severely than in the UNF-MEA [29], despite the increased loading which shifts upward the local polarization curve at low current densities. Increasing air stoichiometry is hence foreseen to improve local performance at <u>cathode outlet</u>; however, this

was demonstrated in [29] to be counter-effective on UNF-MEA <u>cathode inlet</u> performance, worsening local dehydration status.

Simulating I-V distribution at increasing cathode stoichiometry, as in Figure 2C and D ($\lambda_C$=3.4 and 3.6 respectively), the performance gain at <u>cathode outlet</u> region (yellow curve) is noticeable, interestingly without any detrimental effect on dehydrated regions (e.g. <u>cathode inlet</u>, green curve), thanks to the increased local ionomer and catalyst loading. In this way, calculations show that an actual reduction of $\varepsilon_i$ index is possible for the PRB-MEA, reaching a more homogeneous distribution of current density, enabling also the possibility to control current redistribution during actual operation.

*Figure 2. Simulated catalyst loading profiles for UNF-MEA and optimized PRB-MEA (A), together with simulated local I-V curves for the PRB-MEA in counter-flow configuration at nominal conditions $\lambda_C=3$ (B) and with increased cathode stoichiometry to $\lambda_C=3.4$ (C) and $\lambda_C=3.9$ (D). Point of minimum heterogeneity is highlighted in purple.*

The presented modeling analysis reveals that by combining proper CCL loading distribution with fine-tuned cathode stoichiometry, it is possible to actively control both current density distribution and its homogeneity, as highlighted in Figure 3B-D.

### 4.1.2 Gradient CCL manufacturing

In order to validate model predictions, in the following the PRB-MEA is manufactured and experimentally characterized in the m-SFC setup. The PRB-MEA has been manufactured by EWII Fuel Cells A/S. The most proper technique to control the local loading of catalyst, carbon and ionomer has been identified in regulating local electrode thickness. Thus, in the catalyst coated membrane (CCM) manufacturing process, deposition time of the different regions have been locally varied depending on the desired local loading value. The strategy permits to maintain unchanged Pt/C and Ionomer/C ratios also without altering structure of the electrode such as the porosity. Figure 3 reports SEM MEA cross-section images, highlighting the different thickness for the different regions. A thickness of about 40 μm is measured at underline cathode inlet and outlet areas, where loading is increased, while measured thickness at cathode center is about 20 μm.
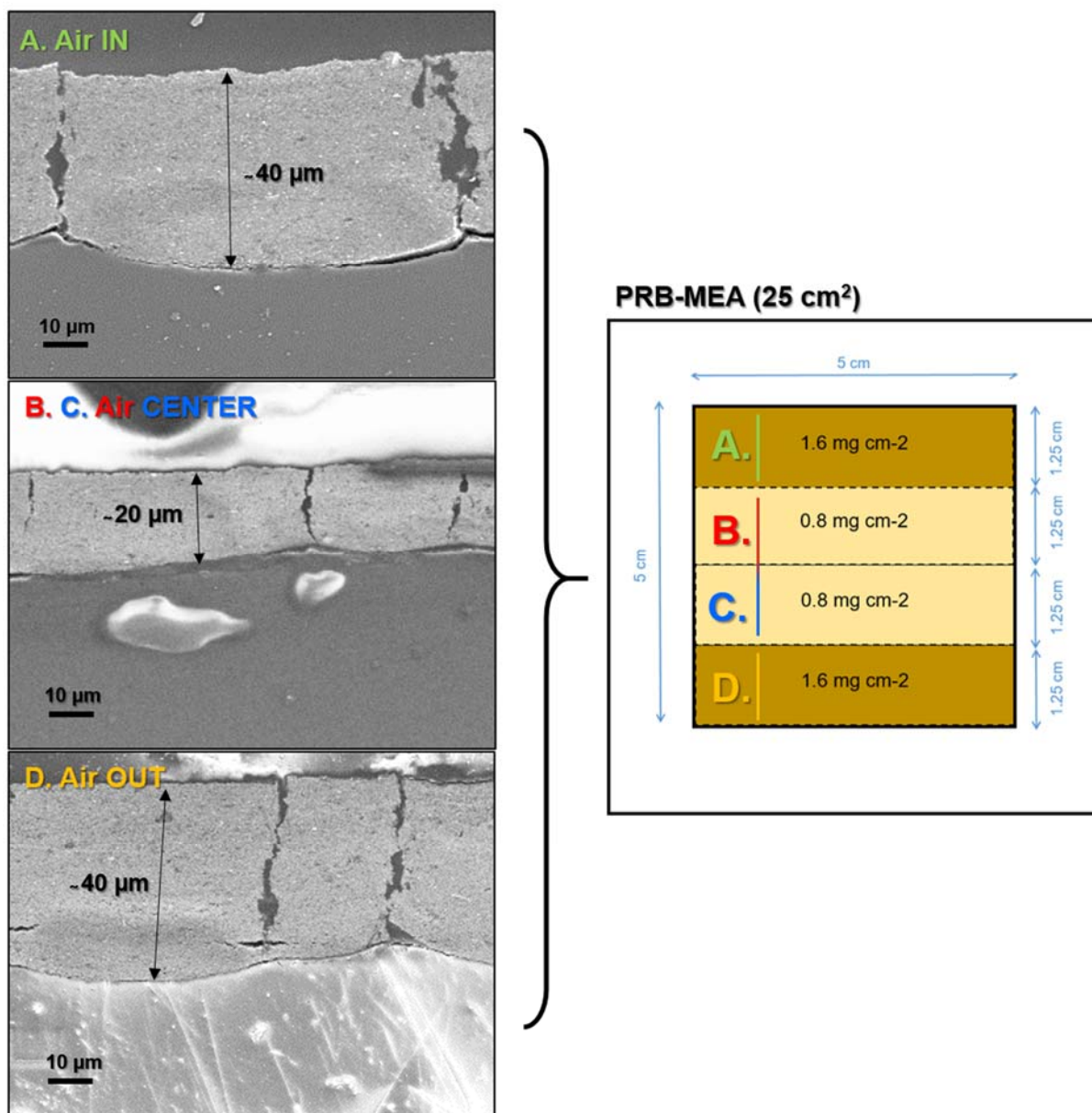
*Figure 3. Scheme of PRB-MEA catalyst/ionomer loading regions together with SEM images of cathode cross-sections observed of air inlet (A), air center (B and C) and air outlet (D), highlighting CCL thickness.*

Preliminary local CV testing on the PRB-MEA were performed on the m-SFC setup, confirming the varying local loading of the component (relative voltammogram is reported in the supplementary materials). The measurements reveal increased charge associated with the hydrogen adsorption-desorption processes from CCL (0.08-0.35 V) as well as increased double-

layer capacitance, proportionally to the increased thickness of the regions. However, on the other hand, calculating the electrochemical surface area (ECSA) considering the different loading as in Table 1, higher loading segments reveal slightly lower ECSA values, which is most likely due to slightly lower catalyst accessibility at BoL.

*Table 1. Calculated cathode ECSA values of PRB-MEA activated sample*

| Cell segment | Air IN | Air IN-MID | Air MID-OUT | Air OUT |
|---|---|---|---|---|
| CL [$mg_{Pt}$ cm$^2$] | 1.6 | 0.8 | 0.8 | 1.6 |
| ECSA [m$^2$ g$^{-1}$] | 25.82 ±1.29 | 28.71 ±1.44 | 28.18 ±1.41 | 26.45 ±1.32 |

### 4.2    PRB-MEA steady state testing

Local current density and impedance distribution of PRB-MEA has been measured analogously to the UNF-MEA [29]. However, it is worth reporting that, surprisingly, no noticeable effect on overall cell performance is distinguishable between UNF-MEA [29] and PRB-MEA in nominal operating conditions. Indeed, comparing global I-V curves of multiple MEA samples, just a 5 mV difference at 0.25 A cm$^{-2}$ is noticeable (as reported in supplementary materials), comparable with measurement uncertainty. This confirms again the importance of local performance analysis, which reveals instead important differences between the MEAs, as it will be clarified in the following.

To verify the impact on PRB-MEA performance distribution related to variations of cathode stoichiometry, local I-V curves measured varying cathode stoichiometry have been measured and are reported in Figure 4.
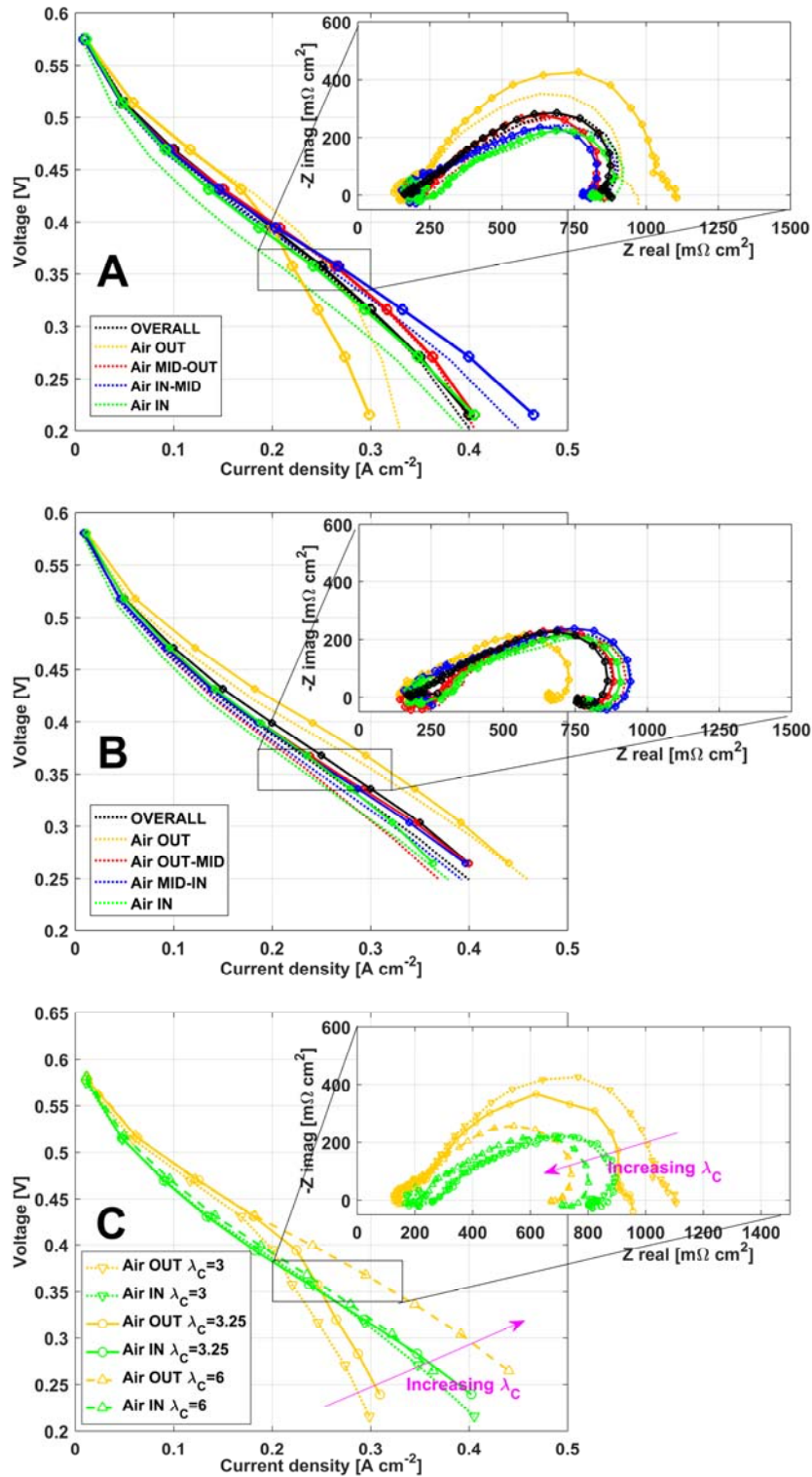
*Figure 4. Overall (black) and local (colored) I-V curves, together with 0.25 A cm$^{-2}$ local EIS, measured in A) reference operating conditions and B) $\lambda_C$ increased to 6 at 0.25 A·cm$^{-2}$ (Solid curves: PRB-MEA, dotted curves: UNF-MEA from [29]). C) Effect of increasing $\lambda_C$ from 3 to 3.25 to 6 on PRB-MEA local I-V curves and EIS at air inlet (green) and outlet (yellow) regions.*

### 4.2.1   Reference conditions

Figure 4A reports local I-V curves performed in reference operating conditions (as described in section 2.2) and the local EIS performed at the reference current density (0.25 A cm$^{-2}$). Despite the slightly variation of global performance (black curve) from that of the UNF-MEA [29], just discussed, local current density and impedance show a sensible redistribution leading to $\varepsilon_i$=18.8% from 21.7% [29]. In particular:

- Air inlet area (depicted in green) I-V curve is sensibly improved from that of UNF-MEA, being for the PRB-MEA almost superimposed to the average MEA performance, already from the lowest current density points. At reference current density (0.25 A cm$^{-2}$), this region is delivering 0.242 A cm$^{-2}$ (-3%), strongly improved from the 0.212 A cm$^{-2}$ (-15%) of the UNF-MEA case [29].

  Comparing PRB-MEA local EIS with that of UNF-MEA [29], a 15% shorter 45° linear branch feature and a 5% lower HFR value are revealed, indicating respectively an improved proton transport across the catalyst layers and polymer membrane [50,51]. This finally leads to a lower LFR, consistent with a lower slope of the I-V curve [52].

- Air outlet area (depicted in yellow) show instead a decrease in performance with respect of UNF-MEA, revealing a drop in I-V already from 0.2 A cm$^{-2}$, which makes this region the performance limiting one from 0.25 A cm$^{-2}$ on. Local EIS spectra indicates mass-transport limitations leading the region to the highest LFR value among all the segments (1,112 m$\Omega$ cm$^2$), consistently with the local I-V curve increased slope.

Measurements confirm modelling simulation discussed in section 4.1.1. Increased catalyst and ionomer loading actually promote ORR rate at cathode inlet area, despite the locally

dehydrated conditions that were hindering local performance of UNF-MEA discussed in [29], most likely due to a self-hydration mechanism. An additional effect, that would require dedicated investigations, might be related to the increased water retention promoted by a thicker CL. However, as reported in [43], the reaction penetrates throughout CL thickness and thus the improved hydration in the thicker CL is expected to be mainly related to the increased water production induced by ORR. This is also confirmed comparing I-V curve at cathode inlet (Figure 4A): in PRB-MEA the I-V curve is translated upwards with respect to the UNF-MEA even at low current densities, suggesting that the increased thickness of the CCL is actually active.

However, on the other side this appears to have a detrimental effect at cathode <u>outlet region</u>, consistently with modelling simulation discussed in section 4.1.1. In this regard it is to be kept in to account that, while the total oxygen consumption and water production (mainly related to the overall current density value) keep unvaried, their distribution on cathode electrode sections change from UNF-MEA case according to local current density distribution. Thus, the discussed beneficial increase of local current density at <u>cathode inlet</u> of the PRB-MEA, leads to increase the reactant consumption and products generation localized in this area. Hence, cathode air feeding reaches the last portions of PRB-MEA poorer in oxygen and richer in water than in the UNF-MEA case, hindering <u>cathode outlet</u> performance despite the discussed locally increase of catalyst and ionomer loading.

### 4.2.2 Increased cathode stoichiometry

Figure 4B shows local I-V curves and local EIS spectra measured for the PRB-MEA operated with doubled cathode stoichiometry at nominal current density ($\lambda_C$=6 at 0.25 A cm$^{-2}$), analogously to what already did for the UNF-MEA [29]. Comparing the overall cell I-V curve (depicted in black in Figure 4B) with that of the UNF-MEA, an improved performance in the whole investigated current density range is evident (10 mV gain at 0.25 A cm$^{-2}$).

Correspondingly, overall cell EIS show an 8% lower total impedance value, derived from a sensible shortening of the high-frequency linear branch [50,51].

Local analysis reveals an heterogeneity index of $\varepsilon_i$=23.9%, permitting important insights:

- Air inlet area I-V curve and EIS spectra (depicted in green) is close to the cell average performance and appears just slightly affected by the $\lambda_C$ doubling. I-V curve slope, EIS HFR value and 45° linear branch [50,51] features are showing just a negligible increase from the nominal operating conditions discussed in section 4.2.1.

- Air outlet area I-V and EIS (depicted in yellow), consistently with the doubled cathode stoichiometry, are showing strongly increased performance from the reference case. The area produces almost 0.45 A·cm$^{-2}$ at a cell average current of 0.4 A·cm$^{-2}$, promoted by the increased local catalyst loading. EIS spectra shows the lowest impedance among all the segments and no mass-transport related feature is noticeable at low frequency.

It is important to recall that, in this conditions, UNF-MEA (discussed in section 3.2.2 of [29]) was demonstrated to develop a strong loss of air inlet local performance, related to increased dehydrating effect driven by increased flow of low-RH air. Together with the improvement of performance at cathode outlet, the condition was leading to unwanted current density heterogeneity increase.

In this case, instead, PRB-MEA does not show any appreciable loss localized in air inlet region. By locally promoting the discussed self-hydration mechanism, air inlet region performance appears to be less sensible to increase of cathode stoichiometry: both local I-V curve and local EIS spectra are not indicating any increased ionomer dehydration effect. Thus, an increase of

$\lambda_C$ is just effective on increasing performance produced by <u>air outlet</u> region, permitting hence to use the parameter to actively control the current density distribution.

### 4.2.3   Optimal cathode stoichiometry

Seen the result of the previous section, an experimental optimization of cathode stoichiometry has been performed, aiming to identify the condition leading to the most homogeneous current density distribution at 0.25 A·cm$^{-2}$. Figure 4C reports local I-V curves and EIS, focusing just on <u>cathode inlet</u> and <u>outlet</u> regions for sake of clarity (respectively depicted in green and yellow), varying cathode stoichiometry. Starting from the reference value ($\lambda_C$=3, discussed in section 4.2.1 and reported as dotted curves) to the doubled value ($\lambda_C$=6, discussed in section 4.2.2 and here reported as dashed curves), the optimal value has been experimentally identified in $\lambda_C$=3.25, represented in solid curves in Figure 4C. This stoichiometry value leads to a current heterogeneity level decreased to $\varepsilon_i$=7.9% at 0.25 A·cm$^{-2}$ that, from $\varepsilon_i$=18.8% and $\varepsilon_i$=21.7% (at $\lambda_C$=3) respectively of the PRB-MEA and the UNF-MEA [29], represents a sensible improvement towards a homogeneously distributed optimal operation.

### 4.3   Local degradation investigation

In order to evaluate the impact on durability of such homogeneous current density distribution, a 500 h degradation test has been repeated in analogy to that of the UNF-MEA [29], after implementation of an optimized operating protocol. In order to avoid as much as possible any non-optimized local operation in critical regions, which may promote early localized fading of performance [29], current density homogeneity has been targeted during operation. As demonstrated in [29], current density follows a spontaneous redistribution during prolonged operation mainly as a consequence of water redistribution, leading to shrinking of the active domain of the MEA. Being cathode stoichiometry effective in controlling current density

heterogeneity as just discussed in section 4.2.3, it will be used to maintain the current density homogenous during operation as described in section 2.2.

Figure 5 shows both cell voltage (A) and current density distribution (B) during 500 h reference discontinuous operation for the PRB-MEA. During each interruption for diagnostics, periodically performed every 100 h as discussed in section 2.2, the necessity to adjust operating conditions is verified, depending on the growth of $\varepsilon_i$ parameter above the target value of 20%.
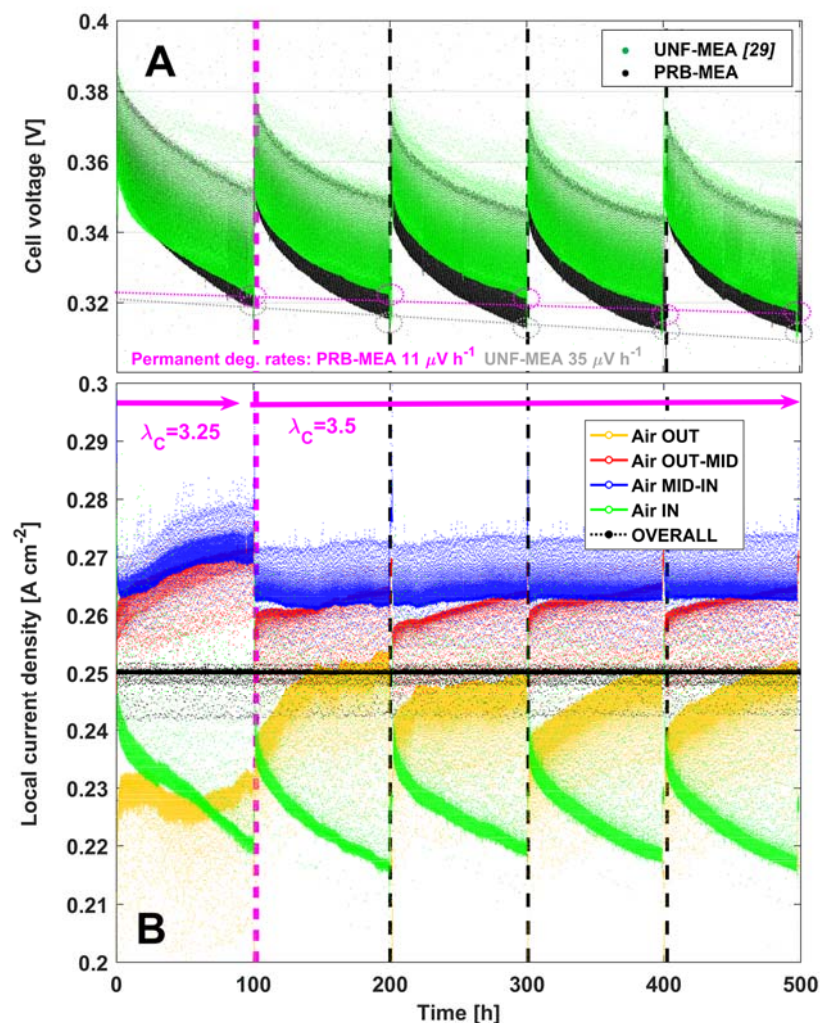


*Figure 5. Cell voltage decay (A) of PRB-MEA (green) with UNF-MEA (from* [29]*), reporting respective permanent voltage decay rate calculation in purple and gray, and local current density of PRB-MEA (B) evolution during a 500 h discontinuous reference degradation test at 0.25 A cm⁻². Purple dotted line indicates operating parameter adjustment.*

Current density heterogeneity at the beginning of the test (0 h in Figure 5) is 45% lower than that of the UNF-MEA [29], consistently with the optimized polarization curve at $\lambda_C$=3.25 discussed in section 4.2.3. As reported in the picture, adaptation of the $\lambda_C$ value was required only after the first 100 h of operation, when current density redistributed reaching an $\varepsilon_i$ index of 23%. As discussed in [29,47], the most of the changes related to modification of water balance take place in the very first operating period, probably due to a localized breakthrough of liquid water across anode MPL towards cathode side. A localized excess of liquid water in CCL, blocked by cathode MPL, can determine mass-transport issues, leading to current redistribution over time as visible during the first 100h operation period. The localized decrease at cathode outlet area (depicted in yellow from 0 to 100 h in Figure 5), has been counterbalanced by slightly increasing from $\lambda_C$=3.25 to 3.5; after this adjustment, no other optimizations of the operating conditions were required.

Considering this optimized operating protocol applied over 500 h, the test reveals a current density redistribution from a minimum heterogeneity level of about $\varepsilon_{i,min}$=10% up to a maximum of $\varepsilon_{i,max}$=20%. This is a sensible improvement from the heterogeneity level exhibited by the UNF-MEA test discussed in [29], exhibiting respectively $\varepsilon_{i,min}$=20% and $\varepsilon_{i,max}$=32%. This indicates a distributed optimal operation, leading to a positive impact on voltage loss: as visible from the comparison of Figure 5B, in 500 h the 35 $\mu V\ h^{-1}$ degradation rate measured for the UNF-MEA in [29], reaches a degradation rate as low as 11 $\mu V\ h^{-1}$ for the PRB-MEA.

This almost 70% decrease of permanent degradation rate requires a deeper discussion. Local ECSA loss measured by means of periodical CV analysis (black solid curve in Figure 6B) reveals a 31% ECSA loss in 500 h, just slightly improved from UNF-MEA (34%) [29]. In good consistency are also ECSA loss trend along the test and the segments local contribution to overall ECSA loss, which appear rather homogeneous. These results, whose consistency with

TEM and XRD analysis will be verified in section 4.4, appear to indicate that the reason for such reduction of degradation rate is not mainly related to global or local ECSA loss reduction.
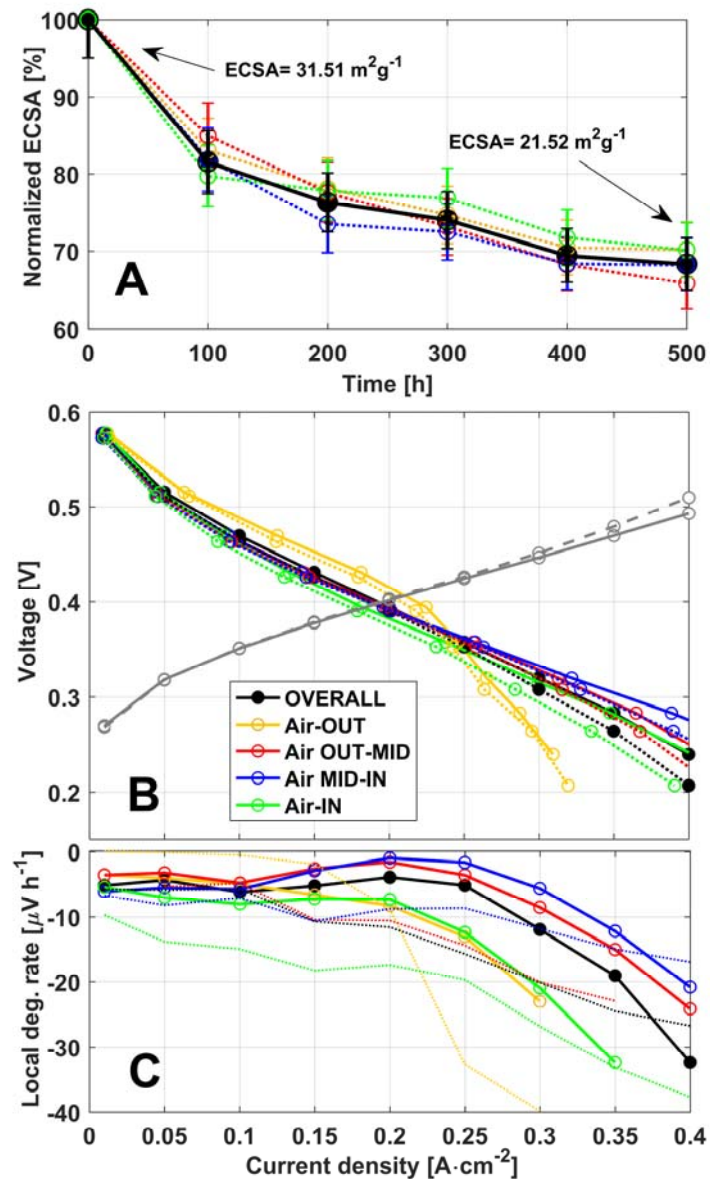


*Figure 6. Local (black curve) and overall (colored curves) ECSA trend during 500 h degradation test, normalized with respect to BoL values (A).*

*Anode (grey curve), overall (black curve) and corresponding local (colored curves) polarization curves performed at BoT (solid lines) and EoT (dotted lines) (B), including corresponding local degradation rates (C). (For an easy comparison, in panel C values of UNF-MEA from [29] are reported as dotted lines).*

Instead, local analysis of performance loss reveals interesting differences from that of the UNF-MEA discussed in [29]. Figure 6A shows the evolution of local I-V curves, distinguishing anode contribution, from BoT (0 h) to EoT (500 h). For an easy discussion, Figure 6B reports the local voltage decay rate calculated as the difference of the BoL and the EoL I-V curves relative to the test duration of both UNF-MEA (dotted curves) [29] and PRB-MEA, which permits to conclude the following:

- The overall decay rate (black curve in Figure 6C) at 0.25 A cm$^{-2}$ corresponds to 10.2 μV h$^{-1}$ of which 3.8 μV h$^{-1}$ due to anode operation. Recalling the results of the UNF-MEA degradation test [29], respectively 31.2 μV h$^{-1}$ and 5.0 μV h$^{-1}$, this represents a 67% reduction of voltage loss calculated from I-V curves decay. This reduction is in good agreement with that calculated from voltage during operation, discussed just before, and appears as mostly due to cathode electrode.

- Local contributions reveal a sensibly more homogeneous fading of performance if compared to that of the UNF-MEA [29]:

  o Air inlet area (green curve in Figure 6B) reaches a 24.2 μV·h$^{-1}$ decay at 0.25 A·cm$^{-2}$, sensibly improved from result of the UNF-MEA [29] degradation test (39.6 μV·h$^{-1}$). This region voltage decay is not showing anymore any early loss at very low current density, which was attributed in [29] to degradation of the ionomer content of CCL, due to prolonged dehydrated operation [4,53,54]. This was leading to increased activation losses only noticeable during low-RH operation rather than during fully hydrated CV diagnostics. In PRB-MEA, the improved current density at cathode inlet, promoting self-hydration,

may prevent ionomer durability issues, whose consistency with post-mortem analysis will be verified in section 4.4.2 by means of XPS measurements.

- o <u>Air outlet area</u> (yellow curve in Figure 6B) voltage decay appear this time very similar to that of air inlet region, reaching a value of 24.66 $\mu V \cdot h^{-1}$ at 0.25 $A \cdot cm^{-2}$. Particularly, the stronger decay this region was showing in the UNF-MEA after aging [29] (65.42 $\mu V \cdot h^{-1}$), previously attributed to increased impact of ECSA loss due to flooding operation, is mitigated. This is most likely due to a more effective management of localized water content during the operation and diagnostics, thanks to the increased catalyst loading and air stoichiometry.

- o <u>Cell center region</u> (blue and red dotted curves in Figure 6B) are confirmed to be the lowest fading regions of the MEA, with a voltage loss comprised between 3 and 8 $\mu V \cdot h^{-1}$ at 0.25 $A \ cm^{-2}$. Despite the lower local catalyst and ionomer loading, these regions are confirmed to mostly stable during operation and less critical in terms of localized fading.

Summarizing, degradation rate improvement appears to be related to a homogenous decay of performance, maintaining effective and homogeneous utilization of ECSA, rather than to a reduction of its loss, indicating unvaried fading mechanisms.  Local impact of ECSA loss on performance, which was locally worsened in UNF-MEA [29] at inlet and outlet region of cathode due to dehydration and flooding respectively, have been sensibly homogenized and mitigated.

Consistency of such interpretation with actual components properties fading will be confirmed in the next section by means of post-mortem analyses.

## 4.4 Post-mortem analysis

Analogously to what performed for the aged UNF-MEA [29], in order to highlight any possible impact on material degradation of the adopted improvements, post-mortem analysis has been performed on the 500 h aged PRB-MEA by TEM, XPS and XRD.

### 4.4.1 TEM analysis

In order to analyze the nanoparticle size evolution during the ageing test, TEM analyses were performed on the pristine MEA and on the aged PRB-MEA in the <u>air inlet</u> and <u>air outlet</u> zones. Figure 7 shows bright field STEM images of the BoT cathode (A) and EoT cathode at air inlet (B) and air outlet (C) regions. The mean nanoparticle size distribution is reported in Figure 7D (solid bars), based on the analysis of 500-800 particles, and compared with that of the EoT UNF-MEA (empty bars); Table 2 reports the calculated local mean nanoparticle diameters (UNF-MEA values [29] are reported in brackets).

*Table 2. Mean nanoparticle size of cathode electrode of the PRB-MEA at BoT and EoT in the AIR IN and AIR OUT regions, calculated from the histograms of Figure 7D.*

*(To improve results comparability, values relative to UNF-MEA from* [29] *are reported in brackets)*

| MEAs analysed zones | Pristine | Aged | |
|---|---|---|---|
| | | Air INLET | Air OUTLET |
| Mean nanoparticle diameter (nm) | 3.2 | 4.6 (5.3) | 4.2 (5.5) |
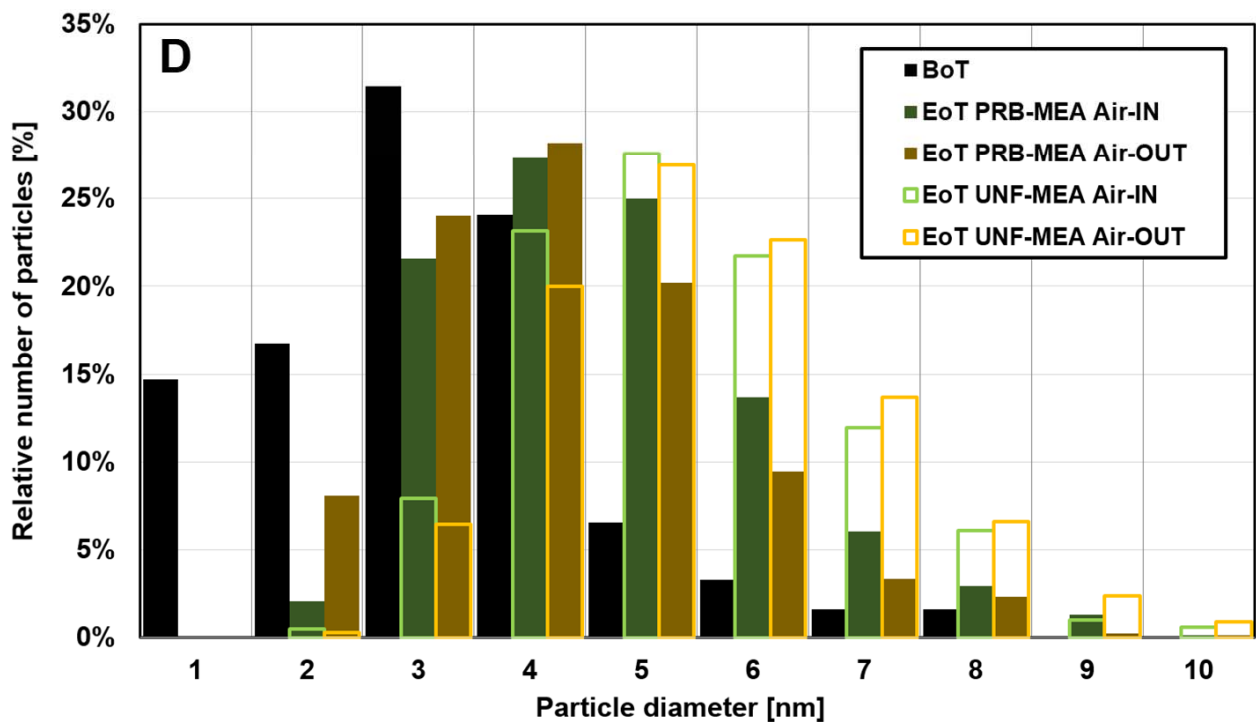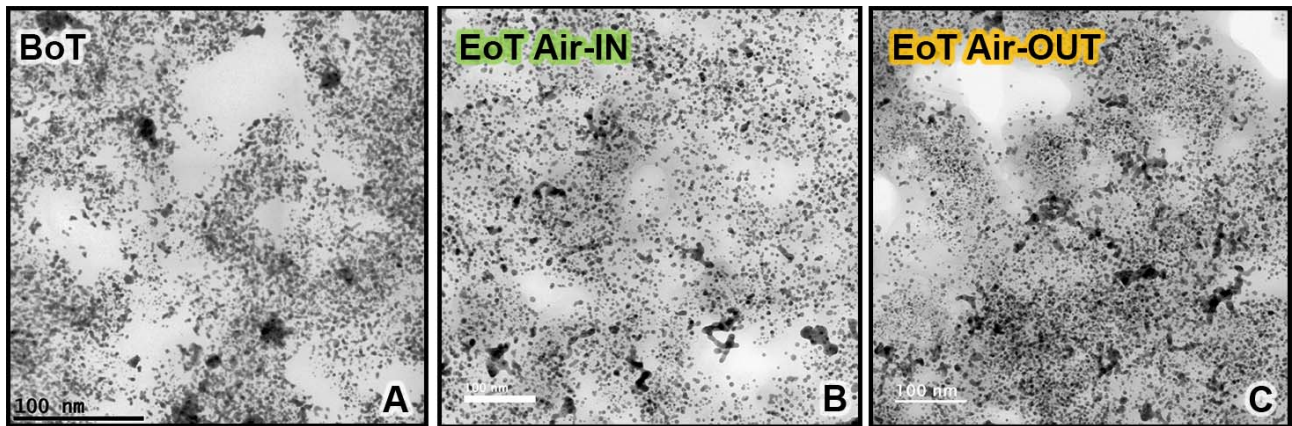
*Figure 7. BF/STEM images of the cathode microstructure of A) the pristine cathode and EoT PRB-MEA at B) air inlet and C) air outlet regions, together with D) relative nanoparticle size distribution. In panel D), also data of UNF-MEA aging test from* [29] *are reported to permit comprehensive comparability of aging test effects.*

These analyses indicate that the 500h ageing test leads to a nanoparticle size increase from an initial mean size of about 3 nm to a final size of about 4 to 4.5 nm, corresponding to an average nanoparticle growth of 50% to 65% that is slightly less than for the UNF-MEA [29]. This nanoparticle size increase results from the electrochemical Ostwald ripening mechanism.

Looking into details, with respect of UNF-MEA [29], the histograms show that in the aged PRB-MEA cathode, less nanoparticle smaller than 3 nm disappeared and less large nanoparticles are formed, resulting from the coalescence of nanoparticle agglomerates observed in the pristine cathode. These two points confirm a slower degradation rate by the electrochemical Ostwald ripening mechanism of the cathode catalyst compared to the UNF-MEA. The origin of this slower degradation rate in the air inlet zone would still require deeper discussion. However, in the air outlet zone, where large water content is expected, the slower degradation rate could be explained by a lower local water content. Indeed, the electrochemical Ostwald ripening mechanism is promoted by a higher ionic conductivity of the ionomer and higher mobility of Pt ions, that are directly linked to the water content [55]. Thus, in the UNF-MEA air outlet zone, the dissolution of almost all the nanoparticles smaller than 3 nm could be related to the discussed local, prolonged cathode flooding. In contrast, in the PRB-MEA air outlet zone, the presence of a quite large number of 2 nm nanoparticles still after 500 h operation suggests lower water content. Thus, the lower degradation rate in the PRB-MEA outlet zone seems to confirm the beneficial effect of the optimized MEA structure and operating strategy both intended to limit cathode flooding accumulation. The analysis can roughly confirm homogeneous fading of cathode CL component, consistent with local CV analysis discussed in section 4.3, revealing strong analogy with UNF-MEA results.

### 4.4.2 XPS and XRD analysis
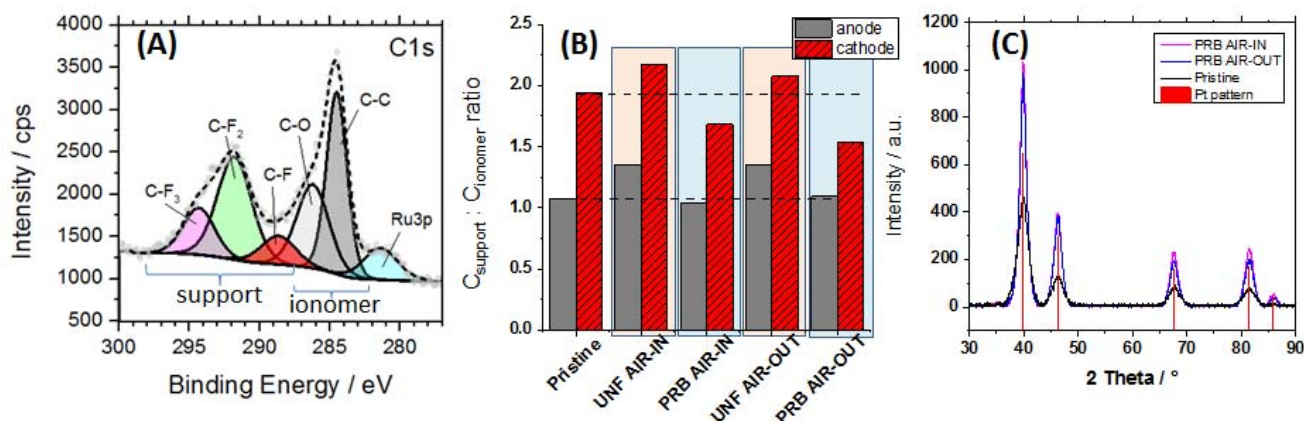


*Figure 8: (A) C1s detailed spectrum with peak deconvolution and assignment. (B) $C_{support}$-to-$C_{ionomer}$ ratio for UNF and PRB samples based in peak assignment from (A). (C) XRD spectra of pristine and PRB electrodes.*

XPS analysis on the EoL sample was performed following the same preparation process applied for the UNF-MEA [29] explained in section 2.4.1. It is worth to mention that, differently from the analysis of the aged UNF-MEA [29] (where anode MPL spontaneously detached from GDL close to the cathode outlet area) PRB-MEA exhibits stronger structural integrity of the GDLs after 500 h testing. This could result from the more homogeneous operation demonstrated in section 4.3 and 4.4.1, where air outlet region was discussed to operate in less harsh flooding conditions.

XPS spectra have been analyzed by deconvolution of the C1s signal as shown in Figure 8A. The assignment is based on correlation of the areas of the fitted C1s peaks with those of S2p, F1s and O1s (not shown). The C1s peaks were used to calculate the $C_{support}$-to-$C_{ionomer}$ ratio, which is plotted in Figure 8B; i.e. the ratio between the sum of peak areas associated with the support and the sum of the peak areas due to the ionomer. Apparently, the AIR-IN and AIR-OUT areas do not show differences within the individual PRB-MEA and the UNF-MEA samples. However, when comparing the UNF and PRB samples, it turns out that there is significant

difference: in the UNF samples C$_{support}$:C$_{ionomer}$ ratio increases for anode and cathode after 500 h operation which was interpreted as related ionomer degradation in [29]. In the PRB samples, on the other hand, a clear decrease of C$_{support}$:C$_{ionomer}$ ratio is observed. This suggests rather carbon corrosion than a pronounced ionomer degradation. Hence, the reduced degradation identified in the PRB-MEA driven by increased platinum and ionomer loading, appears to be also related to its positive impact on degradation of ionomer content, whose operation is most likely less detrimental thanks to reduced dehydration.

According to XRD results in Figure 8 C a decrease of the FWHM af the Pt peaks is observed after operation of which is indicative of Pt crystallite growth. The relative Pt crystallite growth was estimated by determining the FWHMs of the Pt peaks from peak fitting using Pseudo-Voigt function. The FWHM is reciprocal to the average crystallite size according to the Scherrer equation. The calculated relative Pt crystallite growth at AIR-IN and AIR-OUT equals to (41.9±2%) and (40.5±2.5%), respectively. This result is consistent with the observed ECSA loss and shows that ECSA loss is not the main factor leading to performance loss over time.

**Conclusions**

The promising results discussed in this work confirmed that durability improvement in DMFC is achievable by avoiding locally detrimental operating conditions that can induce polymer dehydration and electrode flooding. These phenomena, mainly related to water transport mechanisms, were already identified to respectively enhance performance loss at cathode inlet and outlet of the UNF-MEA [29]. In this work a redistribution of cathode catalyst and ionomer loading was performed with the aim to improve performance of penalized MEA regions, leading to a more homogeneous current density distribution. The design of CCL loading distribution, properly assisted by model simulations, highlighted a 33% increase at cathode

inlet and outlet area together with a 33% decrease at cathode center as the most effective loading redistribution to achieve homogeneous current distribution.

Steady-state local performance analysis of such PRB-MEA confirmed 63% more homogeneous current density distribution at nominal current density (0.25 A cm-2), in agreement with modelling simulations. Performance of cathode inlet region was sensibly improved by avoiding local dehydration, as confirmed from local EIS, mainly thanks to increased water production by ORR. Regulation of cathode stoichiometry value was revealed to mainly affect local performance at cathode outlet region, permitting hence to actively control overall distribution of current density during cell operation.

The impact of CCL variable loading on durability has been assessed in 500 h operation test with local diagnostics, revealing up to 60% more homogeneous current density distribution compared to UNF-MEA [29], leading to 70% lower degradation rate (11 $\mu$V h$^{-1}$). Electrochemical analysis confirmed that PRB-MEA went through homogeneous cathode ECSA loss, this time evenly impacting local performance degradation. Ex-situ post-mortem analyses revealed that the homogeneous operation mitigated the local fading mechanisms: reduced ionomer degradation in CCL and 20% lower nanoparticle growth, homogeneously distributed, have been measured by XPS and TEM respectively. These evidences are in agreement with a locally improved water management during operation, possibly avoiding detrimental ionomer dehydration as well as severe water flooding, which is known to promote catalyst agglomeration.

The methodology discussed in this work, also being demonstrated on commercial scale MEA and hydrogen PEM fuel cell, does not aim to be exhaustive nor definitive, proposing and demonstrating a first step of a more refined local optimization process. Further improvements

are expected to be achievable through local optimization of mass-transport and hydrophobic properties of diffusion layers.

**Acknowledgements**

**Bibliography**

[1]     X. Li, A. Faghri, Review and advances of direct methanol fuel cells (DMFCs) part I: Design, fabrication, and testing with high concentration methanol solutions, J. Power Sources. 226 (2013) 223–240. doi:10.1016/j.jpowsour.2012.10.061.

[2]     M. Sajgure, B. Kachare, P. Gawhale, S. Waghmare, G. Jagadale, Direct Methanol Fuel Cell: A Review, Int. J. Curr. Eng. Technol. INPRESSCO IJCET Spec. Issue. 6 (2016) 2277–4106.

[3]     P. Joghee, J.N. Malik, S. Pylypenko, R. O'Hayre, A review on direct methanol fuel cells – In the perspective of energy and sustainability, MRS Energy Sustain. 2 (2015) E3. doi:10.1557/mre.2015.4.

[4]     F. Bresciani, C. Rabissi, M. Zago, P. Gazdzicki, M. Schulze, L. Guétaz, S. Escribano, J.L. Bonde, R. Marchesi, A. Casalegno, A combined in-situ and post-mortem investigation on local permanent degradation in a direct methanol fuel cell, J. Power Sources. 306 (2016) 49–61. doi:10.1016/j.jpowsour.2015.11.105.

[5]     A.M. Zainoodin, S.K. Kamarudin, M.S. Masdar, W.R.W. Daud, A.B. Mohamad, J. Sahari, Investigation of MEA degradation in a passive direct methanol fuel cell under different

modes of operation, Appl. Energy. 135 (2014) 364–372. doi:10.1016/j.apenergy.2014.08.036.

[6]   R. Escudero-Cid, J.C. Pérez-Flores, E. Fatás, P. Ocón, Degradation of DMFC using a new long-term stability cycle, Int. J. Green Energy. 12 (2015) 641–653. doi:10.1080/15435075.2013.867269.

[7]   N. Kimiaie, K. Wedlich, M. Hehemann, R. Lambertz, M. Müller, C. Korte, D. Stolten, Results of a 20 000 h lifetime test of a 7 kW direct methanol fuel cell (DMFC) hybrid system – degradation of the DMFC stack and the energy storage, Energy Environ. Sci. 7 (2014) 3013–3025. doi:10.1039/C4EE00749B.

[8]   A. Mehmood, M.A. Scibioh, J. Prabhuram, M.G. An, H.Y. Ha, A review on durability issues and restoration techniques in long-term operations of direct methanol fuel cells, J. Power Sources. 297 (2015) 224–241. doi:10.1016/j.jpowsour.2015.07.094.

[9]   F. Bresciani, C. Rabissi, A. Casalegno, M. Zago, R. Marchesi, Experimental investigation on DMFC temporary degradation, Politecnico di Milano, 2014. doi:10.1016/j.ijhydene.2014.09.072.

[10]  C. Eickes, P. Piela, J. Davey, P. Zelenay, Recoverable Cathode Performance Loss in Direct Methanol Fuel Cells, J. Electrochem. Soc. 153 (2006) A171. doi:10.1149/1.2136073.

[11]  J.-Y. Park, M.A. Scibioh, S.-K. Kim, H.-J. Kim, I.-H. Oh, T.G. Lee, H.Y. Ha, Investigations of performance degradation and mitigation strategies in direct methanol fuel cells, Int. J. Hydrogen Energy. 34 (2009) 2043–2051. doi:10.1016/j.ijhydene.2008.10.092.

[12]  C. Rabissi, E. Brightman, G. Hinds, A. Casalegno, In operando investigation of anode overpotential dynamics in direct methanol fuel cells, Int. J. Hydrogen Energy. 41 (2016) 18221–18225. doi:10.1016/j.ijhydene.2016.08.140.

[13]  C. Rabissi, E. Brightman, G. Hinds, A. Casalegno, In operando measurement of localised

cathode potential to mitigate DMFC temporary degradation, Int. J. Hydrogen Energy. (2018). doi:10.1016/j.ijhydene.2018.04.043.

[14]   L.S. Sarma, C.H. Chen, G.R. Wang, K.L. Hsueh, C.P. Huang, H.S. Sheu, D.G. Liu, J.F. Lee, B.J. Hwang, Investigations of direct methanol fuel cell (DMFC) fading mechanisms, J. Power Sources. 167 (2007) 358–365. doi:10.1016/j.jpowsour.2007.02.020.

[15]   Y. Shao-Horn, W.C. Sheng, S. Chen, P.J. Ferreira, E.F. Holby, D. Morgan, Instability of supported platinum nanoparticles in low-temperature fuel cells, Top. Catal. 46 (2007) 285–305. doi:10.1007/s11244-007-9000-0.

[16]   R.L. Borup, D.D. Papadias, R. Mukundan, D. Spernjak, D.A. Langlois, R. Ahluwalia, K.L. More, S. Grot, Carbon Corrosion in PEM Fuel Cells during Drive Cycle Operation, ECS Trans. 69 (2015) 1029–1038. doi:10.1149/06917.1029ecst.

[17]   A. Schröder, K. Wippermann, J. Mergel, W. Lehnert, D. Stolten, T. Sanders, T. Baumhöfer, D.U. Sauer, I. Manke, N. Kardjilov, A. Hilger, J. Schloesser, J. Banhart, C. Hartnig, Combined local current distribution measurements and high resolution neutron radiography of operating Direct Methanol Fuel Cells, Electrochem. Commun. 11 (2009) 1606–1609. doi:10.1016/j.elecom.2009.06.008.

[18]   P. Hartmann, D. Gerteisen, Local degradation analysis of a real long-term operated DMFC stack MEA, J. Power Sources. 219 (2012) 147–154. doi:10.1016/j.jpowsour.2012.07.048.

[19]   D. Dixon, K. Wippermann, J. Mergel, A. Schoekel, S. Zils, C. Roth, Degradation effects at the methanol inlet, outlet and center region of a stack MEA operated in DMFC, J. Power Sources. 196 (2011) 5538–5545. doi:10.1016/j.jpowsour.2011.02.007.

[20]   T. Arlt, I. Manke, K. Wippermann, H. Riesemeier, J. Mergel, J. Banhart, Investigation of the local catalyst distribution in an aged direct methanol fuel cell MEA by means of differential synchrotron X-ray absorption edge imaging with high energy resolution, J.

Power Sources. 221 (2013) 210–216. doi:10.1016/j.jpowsour.2012.08.038.

[21]  L.C. Pérez, L. Brandão, J.M. Sousa, A. Mendes, Segmented polymer electrolyte membrane fuel cells-A review, Renew. Sustain. Energy Rev. 15 (2011) 169–185. doi:10.1016/j.rser.2010.08.024.

[22]  G. Bender, Characterizing Spatial Conditions Within A Hydrogen and Direct Methanol Polymer Electrolyte Fuel Cell Using The Segmented Electrode Approach, Technische Universität München, 2006.

[23]  S.J.C. Cleghorn, C.R. Derouin, M.S. Wilson, S. Gottesfeld, A printed circuit board approach to measuring current distribution in a fuel cell, J. Appl. Electrochem. 28 (1998) 663–672. doi:10.1023/A:1003206513954.

[24]  D.G. Sanchez, T. Ruiu, I. Biswas, M. Schulze, S. Helmly, K.A. Friedrich, Local impact of humidification on degradation in polymer electrolyte fuel cells, J. Power Sources. 352 (2017) 42–55. doi:10.1016/j.jpowsour.2017.03.057.

[25]  M. Schulze, E. Gülzow, S. Schönbauer, T. Knöri, R. Reissner, Segmented cells as tool for development of fuel cells and error prevention/prediagnostic in fuel cell stacks, J. Power Sources. 173 (2007) 19–27. doi:10.1016/j.jpowsour.2007.03.055.

[26]  D.G. Sanchez, A. Ortiz, K.A. Friedrich, Oscillation of PEFC under Low Cathode Humidification: Effect of Gravitation and Bipolar Plate Design, J. Electrochem. Soc. 160 (2013) F636–F644. doi:10.1149/2.091306jes.

[27]  D.G. Sanchez, T. Ruiu, K.A. Friedrich, J. Sanchez-Monreal, M. Vera, Analysis of the Influence of Temperature and Gas Humidity on the Performance Stability of Polymer Electrolyte Membrane Fuel Cells, J. Electrochem. Soc. 163 (2016) F150–F159. doi:10.1149/2.0071603jes.

[28]  J. Shan, P. Gazdzicki, R. Lin, M. Schulze, K.A. Friedrich, Local resolved investigation of

hydrogen crossover in polymer electrolyte fuel cell, Energy. 128 (2017) 357–365. doi:10.1016/j.energy.2017.03.104.

[29]  C. Rabissi, P. Gazdzicki, L. Guétaz, S. Escribano, L. Grahl-Madsen, A. Baricci, A. Casalegno, A locally resolved investigation on direct methanol fuel cell uneven components fading: Steady state and degradation local analysis, J. Power Sources. 397 (2018) 361–373. doi:10.1016/j.jpowsour.2018.07.034.

[30]  B. Bennett, B.M. Koraishy, J.P. Meyers, Modeling and optimization of the DMFC system: Relating materials properties to system size and performance, J. Power Sources. 218 (2012) 268–279. doi:10.1016/j.jpowsour.2012.06.095.

[31]  J. Lee, S. Lee, D. Han, G. Gwak, H. Ju, Numerical modeling and simulations of active direct methanol fuel cell (DMFC) systems under various ambient temperatures and operating conditions, Int. J. Hydrogen Energy. 42 (2017) 1736–1750. doi:10.1016/j.ijhydene.2016.09.087.

[32]  P.A. García-Salaberri, M. Vera, I. Iglesias, Modeling of the anode of a liquid-feed DMFC: Inhomogeneous compression effects and two-phase transport phenomena, J. Power Sources. 246 (2014) 239–252. doi:10.1016/j.jpowsour.2013.06.166.

[33]  Y. Zhang, A. Smirnova, A. Verma, R. Pitchumani, Design of a proton exchange membrane (PEM) fuel cell with variable catalyst loading, J. Power Sources. 291 (2015) 46–57. doi:10.1016/j.jpowsour.2015.05.002.

[34]  Y. Zhang, A. Verma, R. Pitchumani, Optimum design of polymer electrolyte membrane fuel cell with graded porosity gas diffusion layer, Int. J. Hydrogen Energy. 41 (2016) 8412–8426. doi:10.1016/j.ijhydene.2016.02.077.

[35]  N.S. Vasile, A.H.A. Monteverde Videla, S. Specchia, Effects of the current density distribution on a single-cell DMFC by tuning the anode catalyst in layers of gradual

loadings: Modelling and experimental approach, Chem. Eng. J. 322 (2017) 722–741. doi:10.1016/j.cej.2017.04.060.

[36] A. Higier, H. Liu, Optimization of PEM fuel cell flow field via local current density measurement, Int. J. Hydrogen Energy. 35 (2010) 2144–2150. doi:10.1016/j.ijhydene.2009.12.116.

[37] A.A. Kulikovsky, A model for optimal catalyst layer in a fuel cell, Electrochim. Acta. 79 (2012) 31–36. doi:10.1016/j.electacta.2012.06.069.

[38] M.P. Manahan, M.C. Hatzell, E.C. Kumbur, M.M. Mench, Laser perforated fuel cell diffusion media. Part I: Related changes in performance and water content, J. Power Sources. 196 (2011) 5573–5582. doi:10.1016/j.jpowsour.2011.01.014.

[39] F. Bresciani, A. Casalegno, J.L. Bonde, M. Odgaard, R. Marchesi, A comparison of operating strategies to reduce DMFC degradation, Int. J. Energy Res. 38 (2014) 117–124. doi:10.1002/er.3115.

[40] S.K. Roy, M.E. Orazem, Error Analysis of the Impedance Response of PEM Fuel Cells, J. Electrochem. Soc. 154 (2007) B883. doi:10.1149/1.2747533.

[41] J. WU, X. YUAN, H. WANG, M. BLANCO, J. MARTIN, J. ZHANG, Diagnostic tools in PEM fuel cell research: Part I Electrochemical techniques, Int. J. Hydrogen Energy. 33 (2008) 1735–1746. doi:10.1016/j.ijhydene.2008.01.013.

[42] M. Zago, A. Casalegno, F. Bresciani, R. Marchesi, Effect of anode MPL on water and methanol transport in DMFC: Experimental and modeling analyses, Int. J. Hydrogen Energy. 39 (2014) 21620–21630. doi:10.1016/j.ijhydene.2014.03.147.

[43] M. Zago, A. Bisello, A. Baricci, C. Rabissi, E. Brightman, G. Hinds, A. Casalegno, On the actual cathode mixed potential in direct methanol fuel cells, J. Power Sources. (2016). doi:10.1016/j.jpowsour.2016.06.093.

[44] M. Zago, A. Casalegno, C. Santoro, R. Marchesi, Water transport and flooding in DMFC: Experimental and modeling analyses, J. Power Sources. 217 (2012) 381–391. doi:10.1016/j.jpowsour.2012.06.022.

[45] A. Casalegno, F. Bresciani, G. Groppi, R. Marchesi, Flooding of the diffusion layer in a polymer electrolyte fuel cell: Experimental and modelling analysis, J. Power Sources. 196 (2011) 10632–10639. doi:10.1016/j.jpowsour.2011.08.094.

[46] U. Pasaogullari, C.Y. Wang, Liquid Water Transport in Gas Diffusion Layer of Polymer Electrolyte Fuel Cells, J. Electrochem. Soc. 151 (2004) A399. doi:10.1149/1.1646148.

[47] F. Bresciani, C. Rabissi, M. Zago, R. Marchesi, A. Casalegno, On the effect of gas diffusion layers hydrophobicity on direct methanol fuel cell performance and degradation, J. Power Sources. 273 (2015) 680–687. doi:10.1016/j.jpowsour.2014.09.149.

[48] X. Ren, T.E. Springer, T.A. Zawodzinski, S. Gottesfeld, Methanol Transport Through Nafion Membranes - Electro-osmotic Drag Effects on Potential Step Measurements, J. Electrochem. Soc. 147 (2000) 466–474. doi:10.1149/1.1393219.

[49] F. Meier, G. Eigenberger, Transport parameters for the modelling of water transport in ionomer membranes for PEM-fuel cells, Electrochim. Acta. 49 (2004) 1731–1742. doi:10.1016/j.electacta.2003.12.004.

[50] A. Baricci, M. Zago, A. Casalegno, A quasi 2D model of a high temperature polymer fuel cell for the interpretation of impedance spectra, Fuel Cells. 14 (2014) 926–937. doi:10.1002/fuce.201300147.

[51] T. Gaumont, G. Maranzana, O. Lottin, J. Dillet, S. Didierjean, J. Pauchet, L. Guétaz, Measurement of protonic resistance of catalyst layers as a tool for degradation monitoring, Int. J. Hydrogen Energy. 42 (2017) 1800–1812. doi:10.1016/j.ijhydene.2016.10.035.

[52]  M. Chandesris, C. Robin, M. Gerard, Y. Bultel, Investigation of the difference between the low frequency limit of the impedance spectrum and the slope of the polarization curve, Electrochim. Acta. 180 (2015) 581–590. doi:10.1016/j.electacta.2015.08.089.

[53]  A.P. Young, J. Stumper, S. Knights, E. Gyenge, Ionomer Degradation in Polymer Electrolyte Membrane Fuel Cells, J. Electrochem. Soc. 157 (2010) B425. doi:10.1149/1.3281899.

[54]  F. Rong, C. Huang, Z.S. Liu, D. Song, Q. Wang, Microstructure changes in the catalyst layers of PEM fuel cells induced by load cycling. Part I. Mechanical model, J. Power Sources. 175 (2008) 699–711. doi:10.1016/j.jpowsour.2007.10.006.

[55]  L. Guétaz, S. Escribano, O. Sicardy, Study by electron microscopy of proton exchange membrane fuel cell membrane-electrode assembly degradation mechanisms: Influence of local conditions, J. Power Sources. 212 (2012) 169–178. doi:10.1016/j.jpowsour.2012.03.096.